Full Length Article

Why shale permeability changes under variable effective stresses: New insights

Guanglei Cui[a,b], Jishan Liu[c,d,*], Mingyao Wei[a], Rui Shi[e,a], Derek Elsworth[f]

[a] State Key Laboratory of Geomechanics and Geotechnical Engineering, Institute of Rock and Soil Mechanics, Chinese Academy of Sciences, Wuhan 430071, China
[b] University of Chinese Academy of Sciences, Beijing 100049, China
[c] IRC for Unconventional Geomechanics, Key Laboratory of Ministry of Education on Safe Mining of Deep Metal Mines, Northeastern University, Shenyang 110819, China
[d] School of Mechanical and Chemical Engineering, The University of Western Australia, 35 Stirling Highway, Perth, WA 6009, Australia
[e] Key Laboratory of Tectonics and Petroleum Resources, Faculty of Earth Resources, China University of Geosciences, Wuhan 430074, China
[f] Department of Energy and Mineral Engineering, G³ Center and Energy Institute, The Pennsylvania State University, University Park, PA 16802, USA

ARTICLE INFO

ABSTRACT

Experimental measurements of shale permeability are normally conducted under conditions of constant effective stresses. Based on the theory of poroelasticity, shale permeability in non-sorbing media is determined by the effective stress alone and remains unchanged if the effective stress does not change. This theoretical conclusion contradicts some experimental observations in sorbing media. These enigmatic phenomena are analyzed through a model accommodating gas slippage. This approach can explain why shale permeability is significant at low gas pressure but does not explain the contradiction with poromechanics. In this work, we develop and apply an alternative approach to resolve this dilemma. The model comprises flow within a nanotube capillary embedded within the shale matrix (discrete approach) and allows the evolution of shale permeability to be followed during the processes of shale gas flow. In the formulation, we define four strains: global strain of the shale, fracture-local strain, matrix-global strain, and pore-local strain. Shale permeability is defined as a function of these strains that are, in turn, a consequence of effective stress transfer between the matrix and the fracture systems. This behavior is regulated by the differential compliance of the various components and by gas diffusion from the fracture system to the matrix. We use the strain evolution to define how shale permeability changes with time or gas pressure in the matrix system. We apply the new model to generate a series of shale permeability profiles. These profiles are consistent with experimental observations reported in the literature. Through this study, we demonstrate that the experimental observations can indeed be explained through the inclusion of explicit interactions between shale microstructures and gas transport processes.

1. Introduction

Natural gas recovery from tight shales is a growing world-wide contributor to energy supply due to its significant resource size and improving methods of production. According to the United States Department of Energy, shale gas and tight oil production is projected to increase from 13.6 Tcf in 2015 to 29.0 Tcf in 2040, and the proportion of total U.S. dry natural gas production will grow from 50% in 2015 to 69% in 2040 [1]. Shale gas resides in a complex pore network consisting of organic matter (kerogen) and nanotube scale capillaries [2]. The permeability of nanotube capillaries is a key parameter for gas production as it connects the kerogen matrix with natural fractures [3]. Although a number of experimental and theoretical studies have investigated the permeability of nanotubes, our knowledge remains incomplete.

Experimental measurements of shale permeability are normally conducted under conditions of constant effective stresses. Fig. 1 is a compilation of permeability measurements [4–15] and defines two bouding envelopes. Based on the theory of poroelasticity, shale permeability is determined by effective stress alone. Therefore, there would be no permeability change when the effective stress remains constant. However most experimental data exhibit significant changes [5–9,12–14] under constant effective stresses: the permeability declines initially then remains stable as the pressure increases, as inferred by the lower bound in Fig. 1. Wu [16] had conducted an ingenious experiment to investigate the impact of effective stress on the shale permeability and found that the shale permeability would change under the same effective stress as the gas diffuses into matrix with time.

A number of studies have explored these enigmatic experimental
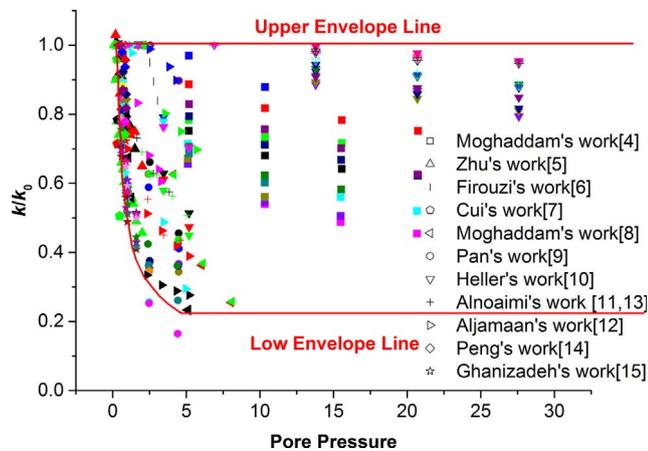
Fig. 1. Experimental measurements of permeability evolution under constant effective stresses.

observations. These studies are normally based on the concept of apparent permeability. As the pores in the shale reservoir are mainly mesopores (2–50 nm) and macropores (> 50 nm) [17,18], these microstructures define the major differences in response from conventional reservoirs: (1) the continuous approximation, characterized by the Knudsen number, may break down [19–21]; and (2) molecular collisions with the pore wall, referred to as gas slippage, becomes nonnegligible [22–23]. The flow regime under such conditions can be described by discrete particle-based atomistic simulations such as Lattice-Boltzmann [24,25], molecular dynamics [26,27] and direct simulation Monte Carlo methods [28]. However the results of these methods are limited to a very short time scale of ps or ns [20,29] and the computations are usually time consuming [30,31]. Such models are only feasible to simulate the nanoscale system rather than realistic field scale [32]. A common approach to resolve this scale issue is to integrate the gas slippage effect with a correlation factor. This approach has been referred to as the apparent permeability approach and was first introduced to shale reservoirs by Javadpour [33]. The apparent permeability is usually defined as the combination of the intrinsic permeability and the gas slippage effect [31,33], commonly shown as: $k = f(Kn)k_\infty$ [34]. $f(Kn)$ represents the correction factor which is often related to the Knudsen number (Kn), and k_∞ represents the intrinsic permeability which depends on the pore structure [35]. Brown et al. [36] introduced a theoretical dimensionless coefficient to correct for slip velocity which is inversely proportional to the gas pressure. Based on his model, many modified formulae have been proposed and used to explain the observed permeability behaviors [37–39]. Recently, other factors such as pore geometry and gas adsorption are considered into apparent permeability model. Naraghi [40] proposed a stochastic, ensemble-based apparent permeability model in which the pore-size distribution and TOC (total organic carbon) were taken into consideration. Also Singh [41] established a Langmuir slip permeability model which accounts for the viscous flow, slip flow, Knudsen diffusion and also the changing of pore diameter due to gas adsorption.

Although the apparent permeability approach has been widely adopted, three major issues remain: (1) The Knudsen number (Kn), originally applied to pipe flow [42,43], must be applied to more complex pore-size distributions that are difficult to accurately characterize in shale reservoir. In addition, we need to consider both the gas flow in the nanotubes but also the complex mass exchange between these tubes and the kerogen; (2) The apparent permeability is measured based on a continuous macro-scale approach while the slippage effect is a microscopic description of the fluid flow at nano-scale; (3) The slippage effect is significant only at low gas pressures [44] because it is inversely proportional to the gas pressure. Apparent from the form of Fig. 1, this threshold pressure is 5 MPa. For shale gas reservoirs, typical

abandonment pressures are barely below this magnitude. These issues suggest that the apparent permeability approach may not be appropriate for the evaluation of gas flow in shale. Due to these limitations, although this approach can explain why shale permeability is significant under a low pressure it cannot explain the contradiction with dependencies on effective stress. This knowledge gap defines the goal of this research.

The complex evolution of shale permeability under conditions of constant effective stresses is a macro-scale phenomenon and must be be explained by a macro-scale theory. Gray [45] was the first to consider the impact of matrix shrinkage on the effective horizontal stress under conditions of uniaxial strain. Matrix shrinkage tended to dilate fractures while increased effective stress reduced fracture permeability with continuing gas depletion. Seidle et al. [46] established the relationship between permeability and horizontal stress under conditions of uniaxial strain. In this model, the form of the permeability –vs– pressure curve exhibits a "Langmuir" form with a decrease of horizontal stress. In Chen's model [47], a variable cleat compressibility based on McKee's work [48] was used instead of the constant fracture compressibility in Seidle's model [46] for a better data match. Also the impacts of fracture tortuosity and fracture connectivity on permeability were discussed in his work. Another widely used theoretical permeability model was proposed by Palmer and Mansoori [49]. In his model, the impact of effective stress and matrix swelling/shrinkage were both considered. Shi and Durucan [50] presented a model for pore pressure-dependent permeability. In this model, changes in the permeability with decreasing gas pressure are controlled by the competing mechanisms of fracture compression and matrix shrinkage. Importantly, these models are only applicable under conditions of uniaxial strain. Other models have been proposed to describe the permeability behavior under variable stress conditions. Robertson and Christiansen [51] developed a model which can be applied to reproduce the permeability behavior under biaxial or hydrostatic confining pressures. The permeability is defined as a function of fracture compressibility, elastic matrix strain, and adsorption strain. Zhang et al. [52] proposed a general porosity and permeability model based on the theory of poroelasticity. In this work, the pore volume change induced by effective stress and gas adsorption were both considered. Based on his work, Liu et al. [53] developed a permeability model considering the internal actions between fracture and matrix. The concept of effective strain comprising global deformation and local deformation was proposed in Peng's work [54,55]. In Peng's models, the permeability can be described as function of effective strain. Recently many researchers have combined models of gas slippage and deformation to represent the evolution of permeability. Pan et al. [9] incorporated the impacts of effective stress and Klinkenberg effect to investigate the impact of anisotropic permeability on experimental observations and shale gas production. Wang and Marongiu-Porcu [56] proposed a unified permeability model for shale gas reservoirs considering gas adsorption effects, compaction effects and the slippage effects. Cao et al. [57] developed an apparent permeability model for shale matrix to investigate the impact of flow regimes and effective stress. Wei et al. [58] presented an apparent permeability model. In his model, the intrinsic permeability is calculated based on the concept of effective strain and the impact of flow regime is based on Knudsen number. Fink et al. [59] investigated the apparent permeability model with the combination of poro-elastic and fluid-dynamic. The stress-dependent permeability can be described by the exponential or power laws and the effect of flow regime was varied with gas slippage factor. The wide variety of macro-scale models are summarized in Table 1.

All of the gas slippage-based models, as reviewed above, can explain why shale permeability changes at low pressures under conditions of constant effective stresses but cannot resolve the contradictions with poromechanics. Based on the theory of poromechanics, shale permeability in non-sorbing media is determined by the effective stress alone and remains unchanged if the effective stress does not change. In this

Table 1
Summary of permeability models.

Author(s)	Expressions	Parameters meaning
Gray [45]	$\sigma_h - \sigma_{h0} = -\frac{v}{1-v}(p-p_0) + \frac{E}{1-v}\frac{\Delta\varepsilon_s}{\Delta p_s}\Delta p_s$	ε_s is the sorption-induced volumetric strain and $\triangle p_s$ refers to equivalent sorption pressure
Seidle et al. [46]	$k = k_0\exp[-3c_f(\sigma_h - \sigma_{h0})]$	c_f is cleat compressibility and σ_h is the horizontal stress
Chen et al. [47]	$k = k_0\exp[-3c_f(\sigma_e - \sigma_{e0})]$ $c_f = \frac{c_{f0}}{\tau(\sigma_e - \sigma_{e0})}(1 - \exp(-\tau(\sigma_e - \sigma_{e0})))$	σ_e is the effective stress and τ is the declining rate of fracture compressibility with increasing effective stress
Palmer and Mansoori [49]	$k = k_0\left[1 + \frac{c_m}{\phi_0}\left(p-p_0\right) + \frac{\varepsilon_L}{\phi_0}\left(\frac{K}{M}-1\right)\left(\frac{p}{p+P_L}-\frac{p_0}{p_0+P_L}\right)\right]^3$ $c_m = \frac{1}{M} - \left(\frac{K}{M}+f-1\right)\gamma$	K is bulk modulus, M is constrained axial modulus, γ is grain compressibility and f is a fraction between 0 and 1
Shi and Durucan [50]	$\sigma_h - \sigma_{h0} = -\frac{v}{1-v}(p-p_0) + \frac{E}{1-v}\varepsilon_L\left(\frac{p}{p+P_L}-\frac{p_0}{p_0+P_L}\right)$	ε_L and P_L are Langmuir constants, E is Young's modulus and v is the Poisson's ratio
Robertson and Christiansen [51]	$\frac{k}{k_0} = \exp\left\{-3c_f\frac{1-\exp[\alpha_c(p-p_0)]}{\alpha_c} + \frac{9}{\phi_0}\left[\frac{1-2v}{E}\left(p-p_0\right)-\frac{\varepsilon_L}{3}\left(\frac{P_L}{P_L+p_0}\right)\ln\left(\frac{P_L+p}{P_L+p_0}\right)\right]\right\}$	α_c is the change rate of fracture compressibility
Zhang et al. [52]	$k = k_0\left(\frac{1}{1+S}\left[\left(1+S_0\right)\phi_0 + \alpha\left(S-S_0\right)\right]\right)^3$	$S = \varepsilon_V + \frac{p}{K_s}-\varepsilon_s$ and $S = \frac{p_0}{K_s}-\varepsilon_{s0}$
Liu et al. [53]	$k_f = k_{f0}\left[1 + \frac{1-R_m}{\phi_{f0}}\left(\Delta\varepsilon_V - \Delta\varepsilon_s\right)\right]^3$	$\triangle\varepsilon_v$ is the volumetric strain and R_m is the modulus reduction ratio
Peng et al. [54,55]	$k = k_0\left(1 + \frac{1}{\phi_0}\Delta\varepsilon_e\right)^3$	ε_e is the effective strain
Pan et al. [9]	$k = k_a\left(1 + \frac{b}{P_p}\right)e^{-3c_f(\sigma - \sigma_0)}$	k_a is the absolute permeability, b is the Klinkenberg constant and σ is the stress
Wang and Marongiu-Porcu [56]	$k = k_a\frac{\left(r_0\left(\frac{\sigma}{\sigma_0}\right)^{-0.5C_\phi} - d_m\frac{p/P_L}{1+p/P_L}\right)}{r_0^2}f(Kn)$	C_φ is a dimensionless material-specific constant [60], r_0 is pore radius and d_m is the average diameter of gas molecules
Cao et al. [57]	$k = k_{\infty0}\exp(-3c_f[(pc-pc0)-(p-p0)]) \times (1+\zeta Kn)\left(1+\frac{4Kn}{1+Kn}\right)$	$k_{\infty0}$ is the intrinsic permeability and ζ is the dimensionless rarefaction coefficient
Wei et al. [58]	$k = k_{\infty0}\left(1 - \frac{\alpha}{\varphi_0}\varepsilon_s\right)^3(1+\zeta Kn)\left(1+\frac{4Kn}{1+Kn}\right)$ $k = k_{\infty0}\left(1 + \frac{\alpha}{\varphi_0}\frac{\Delta p}{K}\right)^3(1+\zeta Kn)\left(1+\frac{4Kn}{1+Kn}\right)$	The upper equation is for the constant volume condition and the lower equation is for the constant stress condition
Fink et al. [59]	$k = k_{\infty0}\exp(\alpha_k\sigma_e)\left[1 + \frac{b}{p}\right]$ $k = k_{\infty1}\left(\frac{\sigma_e}{\sigma_{e1}}\right)^{p_k}\left(1 + \frac{b}{p}\right)$	The upper equation is for the exponential law and the lower equation is for the power law. a_k is an adjustable parameter indicating stress sensitivity, p_k is a power law exponent indicating stress sensitivity and b is gas slippage factor
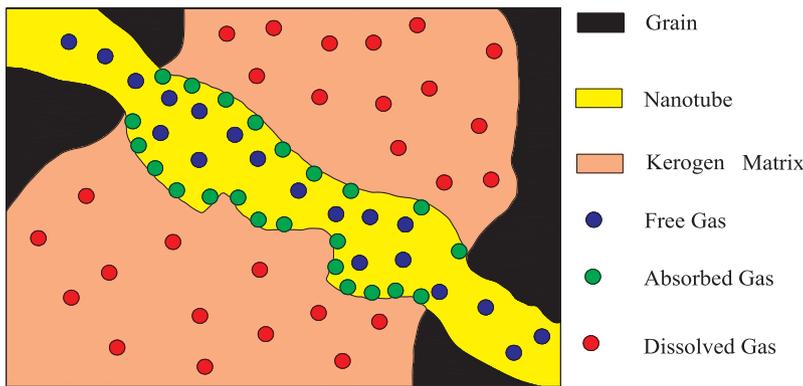
Fig. 2. Schematic illustration of gas distributions in a nanotube-kerogen system [33].

study, we develop an alternative approach to explain widely reported enigmatic experimental observations. We achieve this through the inclusion of explicit interactions between shale microstructures and gas transport processes (discrete approach), and extended this to a continuum approach. For the discrete approach, we model the change in fluid transmission diameter of a nanotube embedded within the shale matrix and relate this change to shale permeability resulting from gas flow. We couple this with a continuum approach based on our previous concepts of local deformation, global deformation and their evolution from the initial equilibrium state to the final equilibrium state. In the formulation, we define four strains: global strain of the shale, fracture-local strain, matrix-global strain, and pore-local strain. Shale permeability is defined as a function of these strains. Its evolution is determined by effective stress transfer between the matrix system and the fracture system, and regulated by the gas diffusion process from the fracture system to the matrix system. Through this study, we demonstrate that the experimental observations can indeed be explained through the inclusion of explicit interactions between shale microstructures and gas transport processes. The new approach and results are reported in the following.

2. Conceptual model

Shale matrix is a typical porous medium which consists of

nanotubes, kerogen and other minerals. Gas is stored in the shale as (1) free gas in nanotubes, (2) adsorbed gas on the surface of nanotubes and (3) dissolved gas in the kerogen [3,61]. A representative nanotube can be used to characterize the heterogeneity of shale structure and gas storage as illustrated in Fig. 2 [33]. During gas production the free gas is first depleted allowing the adsorbed gas and finally the dissolved gas to be depleted. These transport processes occur in series. Gas pressures decline in a similar fashion, decreasing initially in the nanotube(s) and then in the kerogen. The re-distribution of gas pressure in the shale triggers the transition from local deformation to global deformation with both mass transfer and stress transfer. How this transition and the induced strains affect both the gas distribution and the transport properties depend on the external boundary conditions. In this part, we specifically consider two special end-member conditions – those of constant volume and external constant stress. Under conditions of constant volume, we assume that the total volume of the shale remains unchanged throughout the entire depletion process. Under conditions of constant stress, we assume that the confining stresses on the ensemble unit cell remains unchanged throughout the whole process.

2.1. Constant volume condition

As illustrated in Fig. 3, we use the injection of an adsorbing gas (such as CO_2) as an example to illustrate how the mass transfer and the stress transfer between the nanotube and the kerogen are coupled under conditions of constant volume. Prior to injection, the shale is under an equilibrium state (pressure, stress and mass contents) and no interactions between the nanotube and the kerogen occur. Post-injection, a series of processes initiate. First, gas instantly invades the nanotube due to its relatively high permeability. As a result of this process, the gas pressure in the nanotube increases and a pressure difference between the nanotube and kerogen matrix is created resulting in local strain of the nanotube. In this situation, the nanotube swells while the kerogen is compressed as illustrated in Fig. 3(a). Because this occurs only locally, in the vicinity of the nanotube, the swelling volume of the nanotube must be equal the compressive volume of the kerogen. As the gas molecules attach to the nanotube surface and diffuse into the kerogen, local strain evolves in the kerogen matrix due to both the gas adsorption and the increased gas pressure. Under this condition, the kerogen swells while the nanotube shrinks as shown in Fig. 3(b). Because this also occurs locally in the vicinity of the nanotube, the decrease in volume of the nanotube must be equal to the swelling volume of the kerogen. As the gas diffuses further into the kerogen, the gas pressure propagates throughout the kerogen until a new equilibrium state between the nanotube and the kerogen is reached. In this condition, the entire kerogen matrix swells while the nanotube shrinks as shown in Fig. 3(c). Because this occurs globally throughout the kerogen matrix and the total
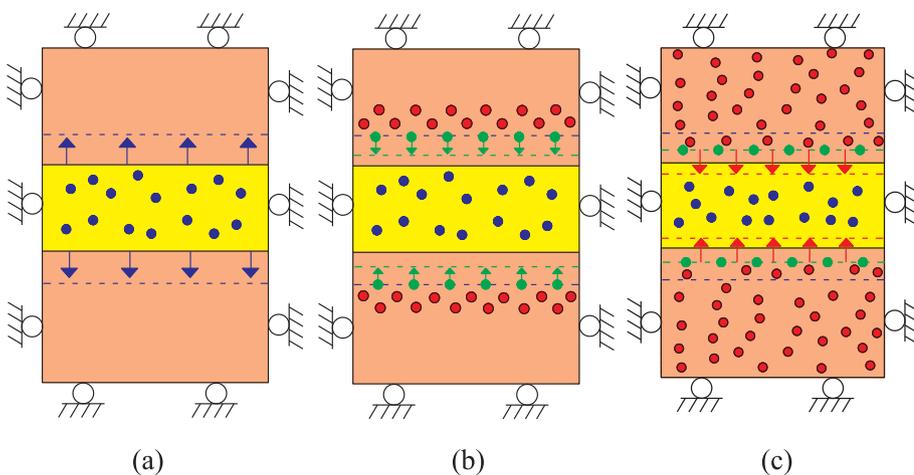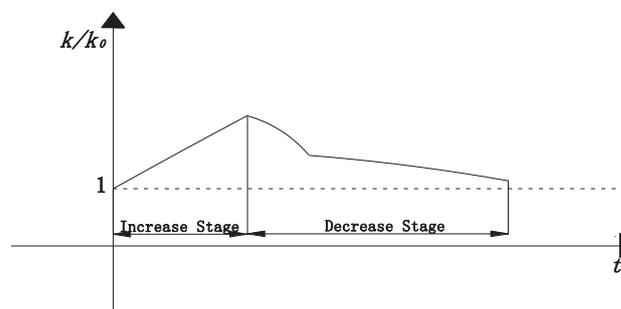
Fig. 4. Evolution of shale permeability under conditions of constant volume.

volume remains unchanged, the decrease in volume of the nanotube must be equal the increase in volume of the kerogen.

The evolution of the nanotube diameter can be transformed into an equivalent shale permeability since the permeability of the nanotube is directly proportional to the square of its radius [62]. As shown in Fig. 4, the shale permeability experiences two distinct stages: (1) Permeability Increase and (2) Permeability Decrease. The stage of permeability increase corresponds to the initial stage of gas injection while the gas rapidly fills the nanotube. When the gas occupies the nanotube, the local strain of the nanotube caused by the increased gas pressure compresses the kerogen. The stage of permeability decrease corresponds to the subsequent progress from gas adsorption to gas diffusion. At this stage, the kerogen matrix swells due to the gas adsorption and the increased gas pressure while the nanotube shrinks.

2.2. Constant stress condition

As shown in Fig. 5, the transition from local deformation to global deformation under conditions of constant stress is also investigated using the injection of an adsorbing gas (such as CO_2). Pre-injection, the shale is in equilibrium and no interactions between the nanotube and the kerogen matrix occur. Post-injection, a sequence of processes progress. Gas pressure in the nanotube increases rapidly due to the relatively high permeability as gas injection begins. As a result, a pressure difference between the two components is created leading to the appearance of nanotube local strain. Under this condition, the nanotube swells while the kerogen shrinks as illustrated in Fig. 5(a). Because this happens locally in the vicinity of the nanotube, the swelling volume of the nanotube is fully transferred to the shrinking volume of the kerogen. As gas molecules adsorb on the nanotube surface and diffuse into the kerogen, the kerogen matrix local strain increases. Under this condition, the kerogen swells while the nanotube shrinks as shown in Fig. 5(b). Because this also occurs locally in the vicinity of the nanotube, the shrinking volume of the nanotube and the swelling volume of
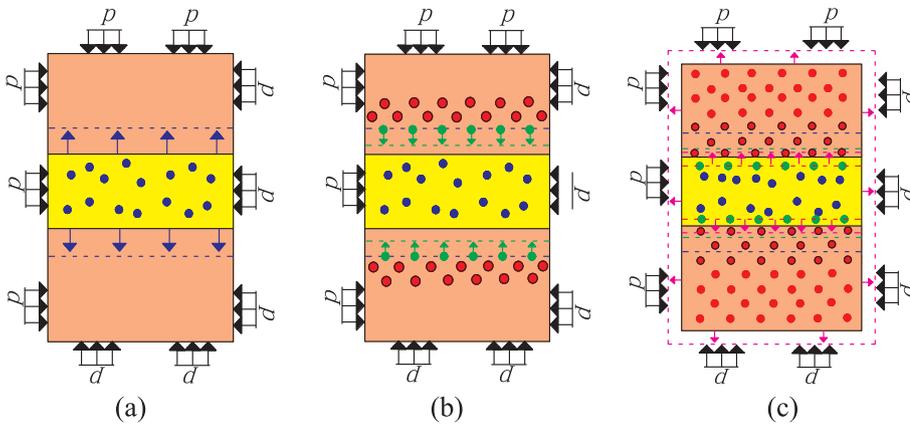
Fig. 3. Illustration of nanotube-kerogen interactions under conditions of constant volume.

(a)   (b)   (c)
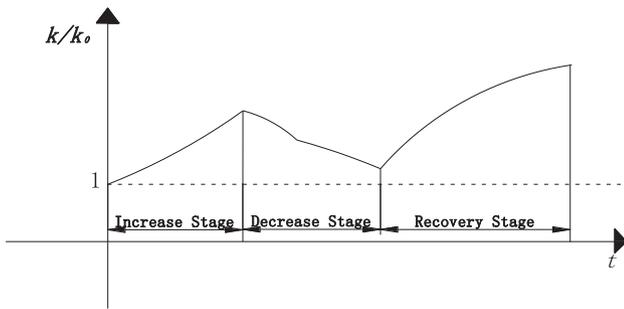
Fig. 6. Evolution of shale permeability under conditions of constant stress.

the kerogen must be equivalent. As the gas diffuses further into the kerogen, the gas pressure propagates into the kerogen until a new equilibrium state is reached. Under this situation, the global strain of the control volume evolves due to the increased gas pressure in the control volume. Because this occurs globally in the shale matrix and the total stress remains unchanged, both the nanotube and the kerogen swell as shown in Fig. 5(c).

The evolution of the nanotube diameter may again be transformed into shale permeability. As shown in Fig. 6, the shale permeability evolves through three distinct stages: (1) Permeability Increase; (2) Permeability Decrease and (3) Permeability Recovery. The stage of permeability increase corresponds to the initial stage of gas injection while the gas instantly fills the nanotube. The nanotube swells due to the increased local strain of the nanotube. The stage of permeability decrease corresponds to the subsequent progress from gas adsorption to gas diffusion. At this stage, the nanotube shrinks due to the local swelling of the kerogen matrix. The stage of permeability recovery corresponds to the stage of shale global deformation. Under the condition of constant stress, the nanotube swells due to the global swelling of shale unit.
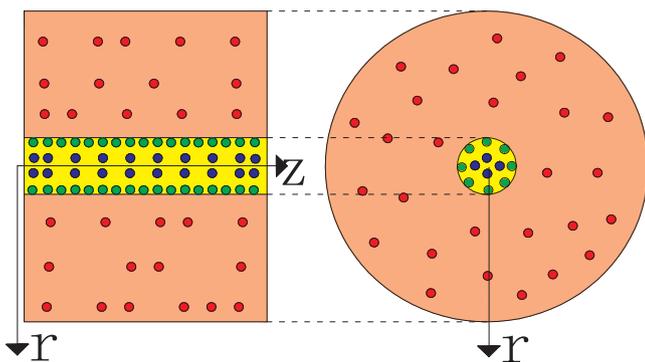
3. Mathematical model

The re-distribution of stresses due to mass transfer and stress transfer result in the dynamic variation of nanotube size and corresponding transport properties. This is the primary goal of this work. Here, a set of partial differential equations (PDEs) are formulated to define the interactions of mass transfer and stress transfer under conditions of swelling-induced stresses.

3.1. Governing equation of the deformation

Considering the influence of pore pressure and adsorption stress, the Navier-type constitutive deformation relation of the control volume becomes [52,63]:

$$Gu_{i,kk} + \frac{G}{1-2v}u_{k,ki} = f_i + \alpha_{np}p_{np,i} + \alpha_{ke}p_{ke,i} + K\varepsilon_{s,i}(p_{sur}) \tag{1}$$

where u is the displacement, p is gas pressure, ε_s is the adsorption strain, α is the Biot coefficient, K is the bulk modulus and G is the shear modulus. The subscripts np and ke represent the nanotube and kerogen matrix, respectively. The subscripts i and k represent the directional components of variables, the subscript kk is the Einstein summation convention and a subscripted comma represents the derivative of a variable. The terms on the right represent the body force per unit volume resulting from gas pressure and adsorption. Meanwhile the heterogeneous swelling process in the matrix [64–66] is also represented as the Young's modulus increases linearly from the nanotube surface to a half radius of the kerogen matrix along the radial direction. Its values at the nanotube surface and at the half radius of the kerogen matrix are βE and E, respectively. Here β is defined as a Young's modulus softening coefficient [67,68].

Applying the Langmuir isotherm yields the gas adsorption strain:

$$\varepsilon_s = \frac{\varepsilon_L p_{sur}}{P_L + p_{sur}} \tag{2}$$

Nanotube

Kerogen Matrix

Free Gas

Absorbed Gas

Dissolved Gas

Fig. 7. Numerical model for permeability change.
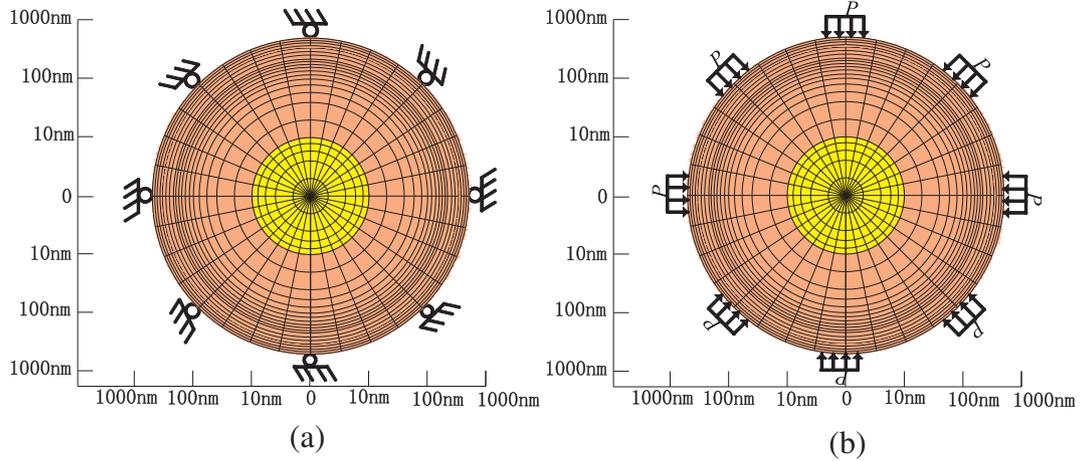
Fig. 8. Illustration of simulation model (a) constant volume condition and (b) constant stress condition.

Table 2
Property parameters of simulation model.

Symbol	Description	Value	Unit
r_{np}	Nanotube radius	10	nm
d_{ke}	Kerogen length	500	nm
μ	Dynamic viscosity	1.84×10^{-5}	Pa·s
ρ_{sh}	Shale density	2600	kg/m^3
ρ_{ga}	Gas density at standard pressure	1.43 (CO_2), 0.18 (He)	kg/m^3
D_{ke}	Kerogen Diffusion coefficient	2.5×10^{-12}	m^2/s
ε_L	Langmuir strain constant	0.02 (CO_2), 0 (He)	–
V_L	Langmuir volume constant	0.03 (CO_2), 0 (He)	m^3/kg
P_L	Langmuir pressure constant	5	MPa
Z	Real gas deviation factor	0.98	–-
H_{dis}	Henry's law constant	7.45×10^{-7}	kg/(Pa·m^3)

where ε_L is the Langmuir strain constant, P_L is the Langmuir pressure constant and p_{sur} is the gas pressure at the nanotube surface. The molecules of adsorbing gas form a dense, liquid like adsorption layer around the nanotube surface and the thickness is equal to the molecular diameter (based on the Langmuir monolayer adsorption theory). In addition to the adsorption layer, there is also a phase transition layer which is approximately twice the diameter of a gas molecule [69], rendering the width of the adsorption region as ~1 nm.

3.2. Gas flow in nanotube

Gas flow in the nanotube is described by Darcy's law and the mass conservation law is:

$$\frac{\partial m_{np}}{\partial t} + \nabla \cdot (\rho_{np} u_{np}) = Q_s \tag{3}$$

where m_{np} represents the mass of gas in the nanotube, Q_s is the source term and u_{np} is the flow velocity in the nanotube which is calculated by Darcy law:

$$u_{np} = -\frac{k_{np}}{\mu} \nabla p_{np} \tag{4}$$

where p_{np} is the gas pressure in the nanotube and k_{np} is the permeability of the nanotube. ρ_{np} is the gas density in the nanotube:

$$\rho_{np} = \frac{p_{np}}{p_{ga}} \rho_{ga} \tag{5}$$

where p_{ga} is standard atmospheric pressure and ρ_{ga} is the gas density at standard atmospheric pressure. Only free gas exits in the nanotube:

$$m_{np} = \rho_{np} \phi_{np} \tag{6}$$

where ϕ_{np} is the porosity in the nanotube.

Thus the gas flow in the nanotube is written as:

$$\frac{\partial}{\partial t} \left(\frac{p_{np}}{p_{ga}} \rho_{ga} \phi_{np} \right) + \nabla \cdot \left(-\frac{p_{np}}{p_{ga}} \frac{k_{np}}{\mu} \rho_{ga} \nabla p_{np} \right) = Q_s \tag{7}$$
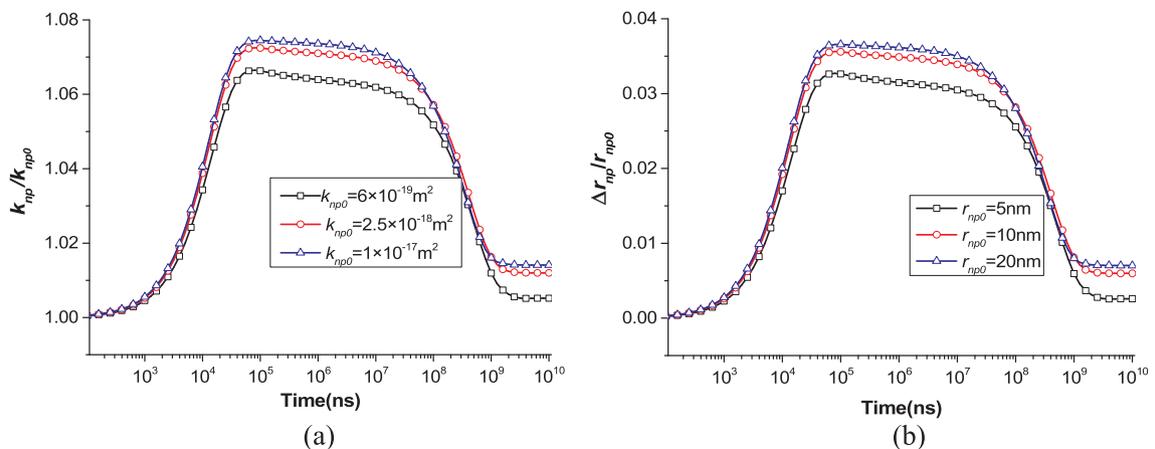
Fig. 9. Evolution of (a) permeability and (b) nanotube radius for non-adsorbing gas (He) under conditions of constant volume.
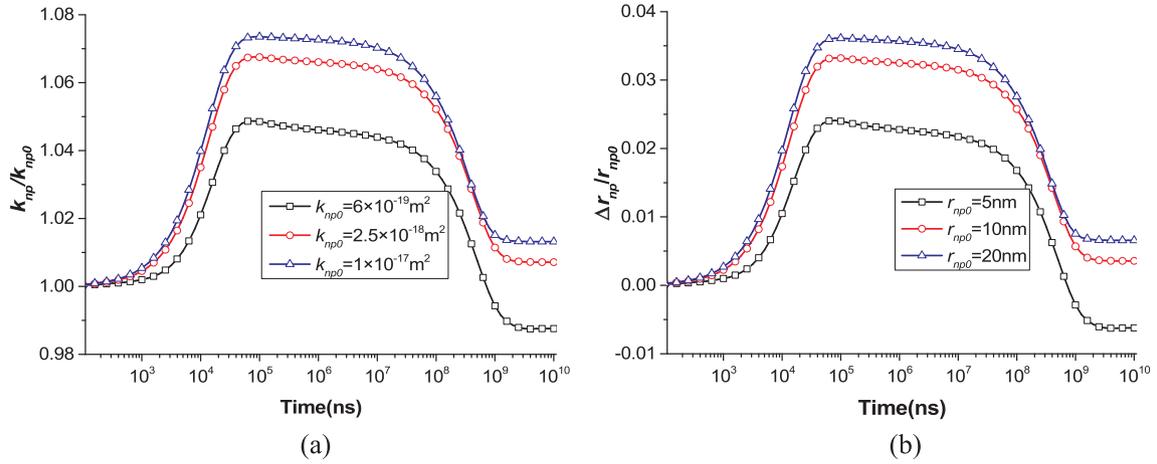
Fig. 10. Evolution of (a) permeability and (b) nanotube radius for adsorbing gas (CO_2) under conditions of constant volume.
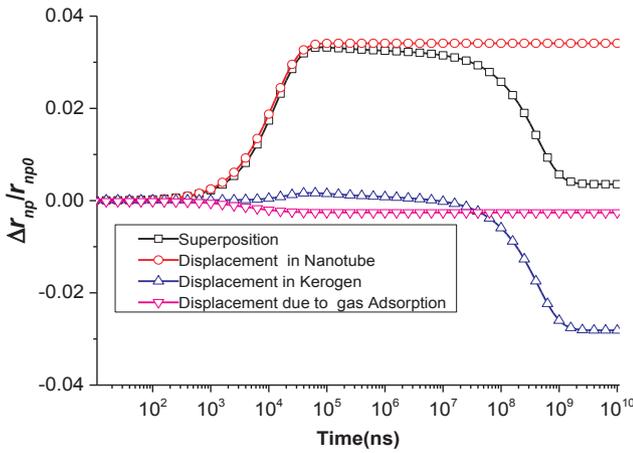
Fig. 11. Contributions of different mechanisms under conditions of constant volume.

3.3. Adsorption/desorption on nanotube surfaces

In this study, the concentration of the absorbed gas (C_{ad}) on the nanotube surface, considering a real gas, is written as:

$$C_{ad} = \frac{V_L p_{sur}/Z}{P_L + p_{sur}/Z} \tag{8}$$

where C_{ad} is the gas concentration on the surface at pressure p_{sur} and Z is the real gas factor.

3.4. The diffusion in kerogen

Kerogen is assumed to surround the nanotube and the dissolved gas in the kerogen begins to diffuse as the concentration gradient appears. The diffusivity equation is written as below:

$$\nabla \cdot (D_{ke} \nabla C_{ke}) = \frac{\partial C_{ke}}{\partial t} \tag{9}$$

where the C_{ke} is the concentration of the dissolved gas in the kerogen and D_{ke} is the diffusion coefficient in the kerogen. Here Henry's law is used to describe the relationship of gas pressure with gas concentration [70,71]:

$$C_{ke} = H_{ke} p_{ke} \tag{10}$$

where H_{ke} is the Henry's constant and p_{ke} is the dissolved gas pressure in the kerogen.

3.5. The permeability model of nanotube

The permeability of the nanotube can be defined as [62]:

$$k_{np} = \frac{1}{\tau} \frac{r_{np}^2}{8} \tag{11}$$

where τ is tortuosity of the nanotube and r_{np} is the radius of the nanotube. The dynamic permeability of the nanotube is expressed as:

$$\frac{k_{np}}{k_{np0}} = \left(1 + \frac{\Delta r_{np}}{r_{np}}\right)^2 \tag{12}$$

Fig. 12. Evolution of (a) permeability and (b) nanotube radius for the case of the homogeneous distribution of Young's modulus under conditions of constant volume.

(a)

(b)
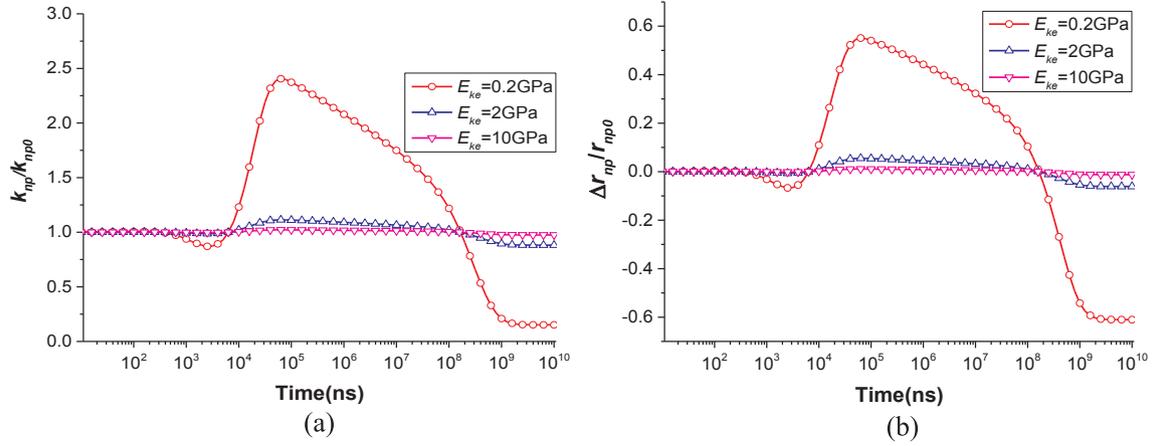
Fig. 13. Evolution of (a) permeability and (b) nanotube radius for the case of the heterogeneous distribution of Young's modulus under conditions of constant volume.
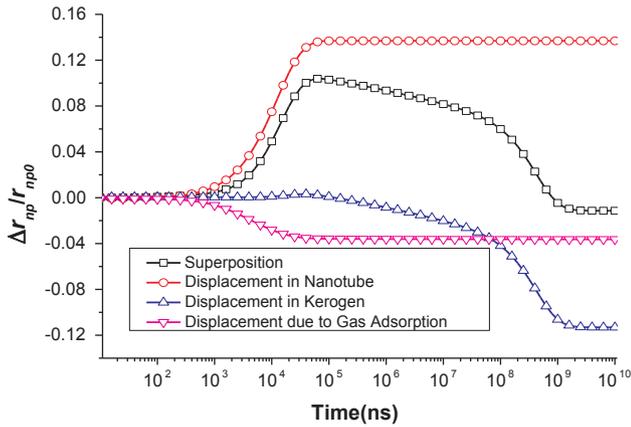
Fig. 14. Contributions of different mechanisms to the variation of nanotube radius for a heterogeneous distribution of Young's modulus at $E_{ke} = 2\,\text{GPa}$ under conditions of constant volume.

where the subscript, 0, denotes the initial value of the variable. The change in radius, $\triangle r_{np}$, depends on the transition from local deformation to global deformation.

4. A heterogeneous kerogen-nanotube interaction model

This fully coupled model is implemented in, and solved by COMSOL Multiphysics (Version 5.2a). In the following section, we apply the model to investigate the evolution of nanotube permeability under two specific boundary conditions – *viz.* constant volume and constant stress.

4.1. Numerical model

In the simulation model, the transition from local deformation to global deformation is investigated under the assumption that the nanotube is embedded in the kerogen matrix as a long cylinder and

creates a full separation between kerogen blocks as shown in Fig. 7. This assumption is also adopted by other studies [70,72]. The axial direction is much longer than the radial direction. A 2D plane strain model is used as shown in Fig. 8. The injection processes of adsorbing gas (CO_2) and non-adsorbing gas (He) are studied as the injection pressure is applied at the center of the nanotube. Representative material properties are applied [70,73–76] as listed in Table 2.

For the mechanical models, the boundary conditions are given as:

$$\mathbf{n} \cdot \mathbf{u} = \mathbf{0} \tag{13}$$

for the constant volume condition as shown in Fig. 8(a) and

$$\mathbf{n} \cdot \boldsymbol{\sigma} = \mathbf{P} \tag{14}$$

for the constant stress condition as shown in Fig. 8(b). Here $\mathbf{u}$ represents the displacement, $\boldsymbol{\sigma}$ represents the stress and $\mathbf{n}$ represents the direction cosine of the normal vector to the boundary.

For the gas flow models, the flow boundary conditions are given as:

$$C_{ad} = \frac{V_L p_{np}/Z}{P_L + p_{np}/Z} \tag{15}$$

on the interface between the nanotube and the adsorption layer, and

$$C_{ad} = C_{ke} \tag{16}$$

on the interface between the adsorption layer and the kerogen matrix.

4.2. Investigation of Permeability Evolution under Conditions of Constant Volume

4.2.1. Evolution of permeability under conditions of constant volume

Fig. 9 and Fig. 10 represent the evolution of permeability and nanotube radius for non-adsorbing (He) and adsorbing gases (CO_2) under conditions of constant volume, respectively. The initial value of the nanotube permeability is estimated from Eq. (11). The variations of the permeability and nanotube radius are attributed to the re-distribution of gas pressure caused by gas injection. The evolution signatures of both the non-adsorbing gas (He) and the adsorbing gas (CO_2) are similar –

Table 3
Simulation scenarios.

Scenario	Adsorption Strain (ε_L, %)	Kerogen Diffusion Coefficient (D_{ke}, m²/s)	Injection Pressure (P_{in}, MPa)	Kerogen Length (d_{ke}, nm)	Biot Coefficient (a_{ke},1)	Results
Case 1	0.1,5,25,50	1×10^{-12}	32.6	500	0.6	Fig. 15 (a)
Case 2	5	$1 \times 10^{-11}, 1 \times 10^{-12}, 1 \times 10^{-13}, 1 \times 10^{-14}$	32.6	500	0.6	Fig. 15 (b)
Case 3	5	1×10^{-12}	5,10,30,50	500	0.6	Fig. 15 (c)
Case 4	5	1×10^{-12}	32.6	100,500,1000, 2000	0.6	Fig. 15 (d)
Case 5	5	1×10^{-12}	32.6	500	0.1,0.4,0.6,1	Fig. 15 (e)
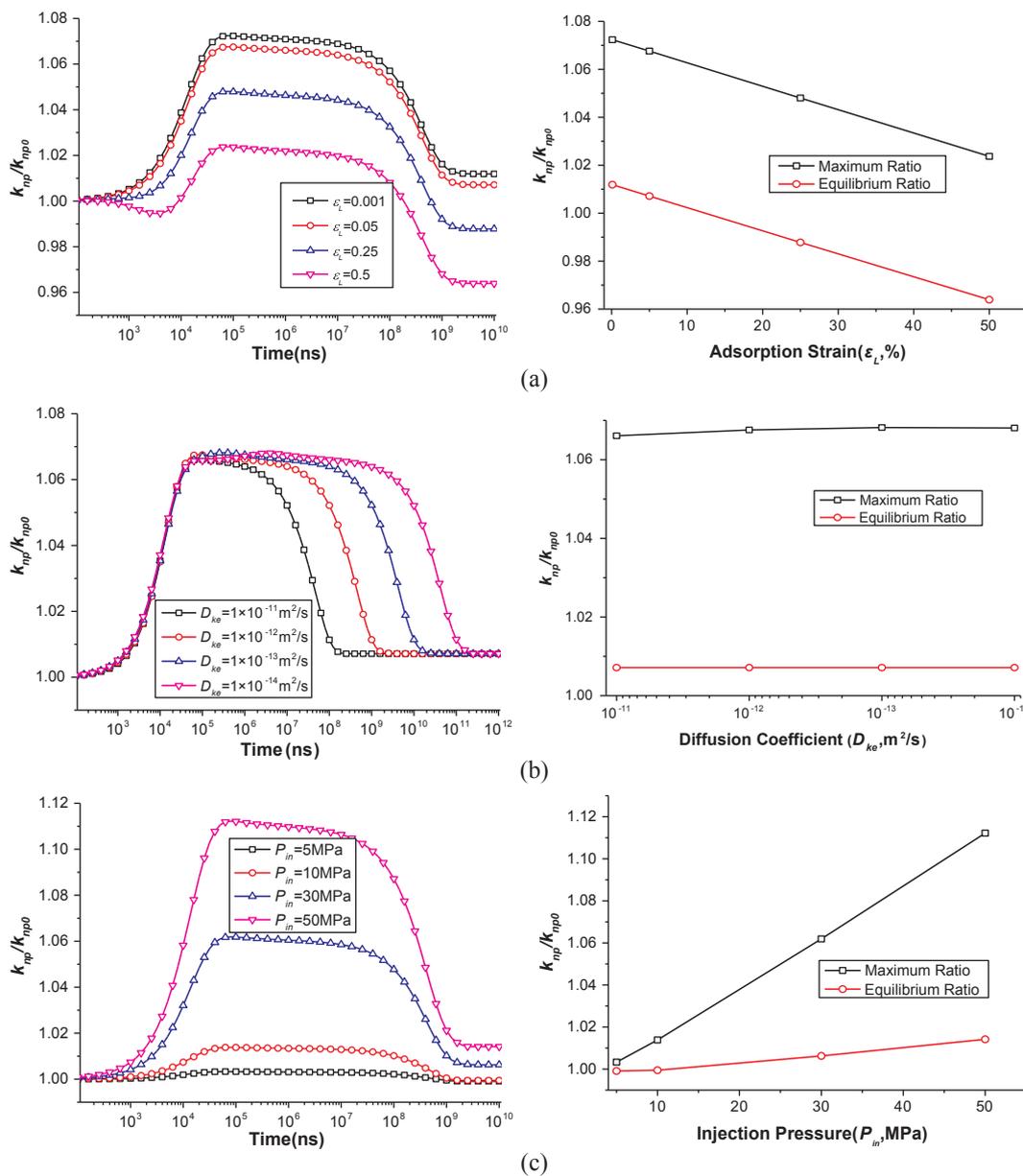
Fig. 15. Influences of (a) adsorption strain (b) kerogen diffusion coefficient (c) injection pressure (d) kerogen length and (e) kerogen Biot coefficient on the variation of permeability under conditions of constant volume.

both experience two stages as discussed in the conceptual model: (1) Permeability Increase. Permeability increases immediately after gas injection as the gas pressure in the nanotube increases while the gas pressure in the kerogen remains at its initial value; and (2) Permeability Decrease. Permeability decreases as the gas contacts the nanotube surface and diffuses into the kerogen matrix. The gas invaded-region swells due to gas adsorption and the increased gas pressure. Through comparing Fig. 9 with Fig. 10, we conclude that the patterns of permeability evolution are similar for different gases but the magnitudes are very different.

The evolution of permeability and nanotube radius are caused by the transition from local deformation to global deformation. Fig. 11 represents the contributions of different mechanisms to the dynamic evolution of interior radius under conditions of constant volume. The stage of increasing radius is mainly due to the nanotube local strain resulting from its increased gas pressure immediately after gas injection. The dynamic change in the radius exhibits a Langmuir form only if the nanotube local strain is considered. This usually occurs when the diffusivity of the kerogen is high and of the same magnitude as the

nanotube permeability. Under this condition, diffusion from matrix to nanotube is not the limiting process and the global deformation determines the evolution of permeability. The stage of radius decrease is mainly due to the swelling strain of the kerogen matrix responding to the increased gas pressure and related gas adsorption. If only the swelling strain of the kerogen matrix is considered, it would exhibit an 'L' shape. Usually the stage of increase is difficult to be captured in experiments due to the high transport capability of the nanotube and that only the impact of the kerogen matrix strain is observed.

4.2.2. Investigation of Young's modulus under conditions of constant volume

The Young's modulus plays a decisive role on the evolution of strain in the kerogen matrix. In this section, the impacts of Young's modulus on the evolution of permeability and nanotube radius are investigated. Two differing distributions of the Young's modulus are considered. The first is that the Young's modulus is uniformly distributed in the kerogen matrix. The second is that the Young's modulus increases linearly from the nanotube surface to the half radius of the kerogen matrix along the

(d)

(e)

Fig. 15. (*continued*)

(a)

(b)
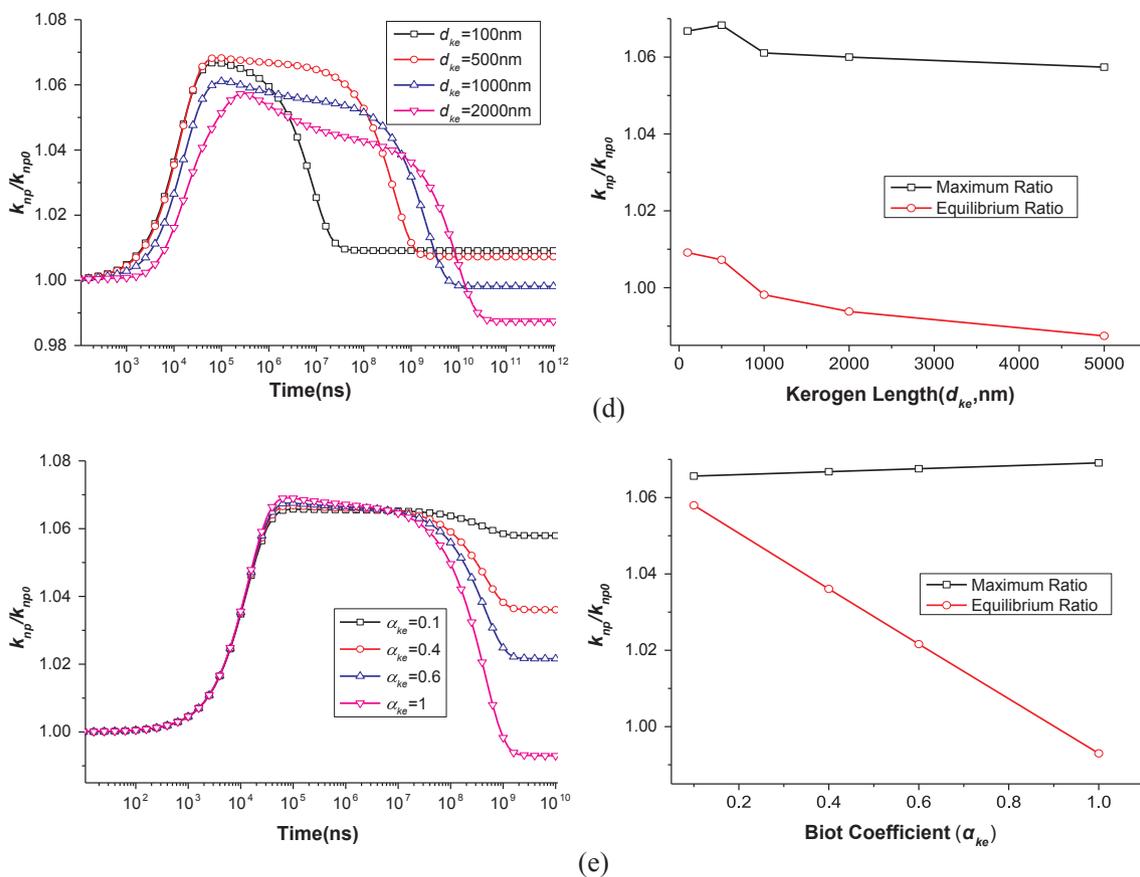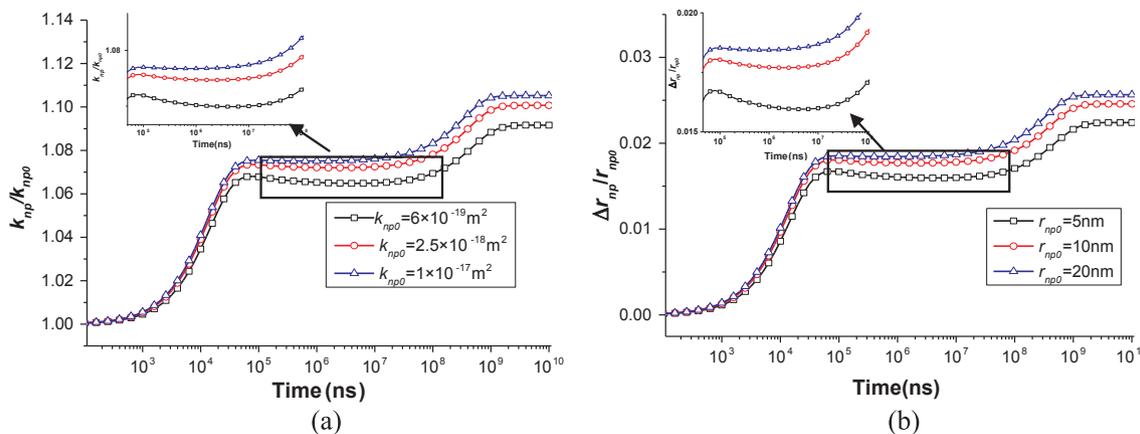
Fig. 16. Evolution of (a) permeability and (b) nanotube radius for non-adsorbing gas (He) under conditions of constant stress.

radial direction [64–66]. The Young's modulus values at the nanotube surface and at the half radius of the kerogen matrix are βE and E [67,68]. Only the injection process of gas adsorption (CO_2) is modelled while the injection of a non-adsorbing gas (He) is treated as the special case of an adsorbing gas ($V_L = 0$ and $\varepsilon_L = 0$).

Fig. 12 and Fig. 13 represent variations in permeability and nanotube radius with the homogeneous and the heterogeneous distributions of the Young's modulus under conditions of constant volume. For the homogeneous case, both the nanotube radius and the permeability exhibit normal patterns but their magnitudes increase as the modulus decreases. For the heterogeneous case, the evolutions of permeability and nanotube radius are much more complex. To determine the reason, the contributions of different mechanisms are illustrated in Fig. 14. Comparing this with Fig. 11 and Fig. 14, we find that deformations are

larger around the nanotube. This is primarily due to the elevated swelling in the kerogen matrix.

4.2.3. Sensitivity analysis under conditions of constant volume

In this section, we investigate the impacts of the Langmuir adsorption strain, the kerogen diffusivity, the injection pressure, the kerogen size, and the Biot coefficient on the evolution of permeability. The kerogen matrix is considered to be homogeneous and the simulation scenarios are listed in Table 3. The results are shown in Fig. 15. For all cases, we plot the permeability evolution as a function of time, and the impacts of each parameter on the maximum permeability ratio and the equilibrium permeability ratio are defined. Patterns of permeability evolution for all cases are similar but magnitudes are different. The impacts of characteristic parameters on the maximum permeability
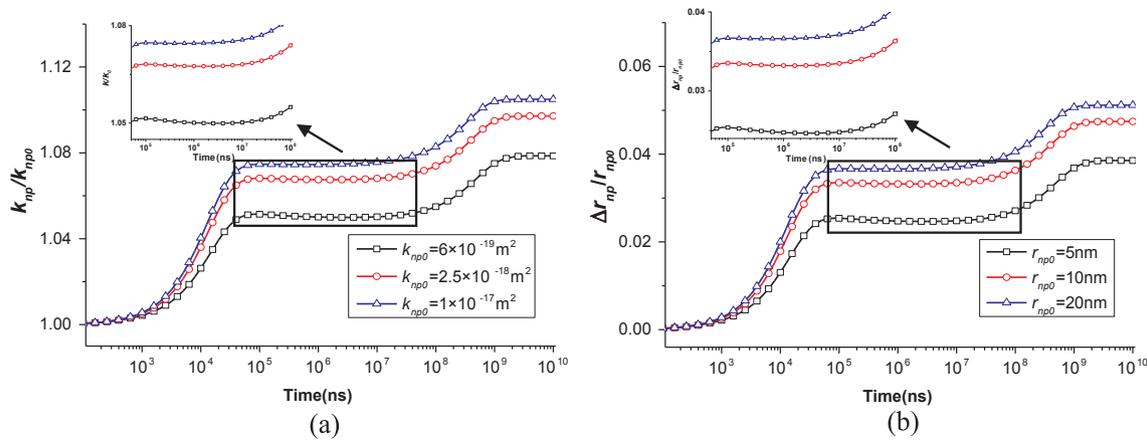
Fig. 17. Evolution of (a) permeability and (b) nanotube radius for adsorbing gas (CO_2) under conditions of constant stress.
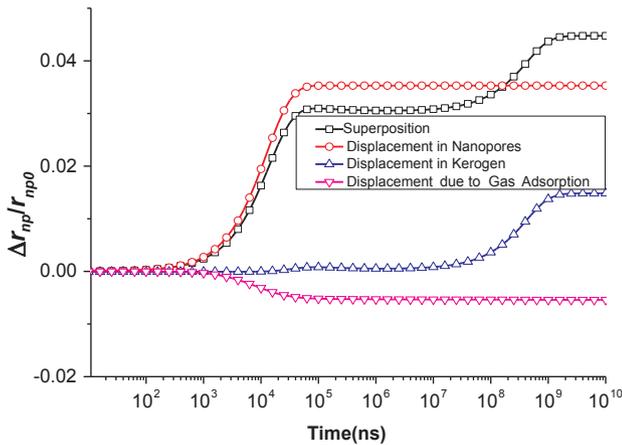
Fig. 18. Contributions of different mechanisms under conditions of constant stress.

ratio and the equilibrium permeability ratio are very different. As shown in Fig. 15(a), both the maximum permeability ratio and the equilibrium permeability ratio decrease linearly as the adsorption strain increases. As shown in Fig. 15 (b), the diffusion coefficient has no impact on either ratio. As shown in Fig. 15(c), both permeability ratios increase linearly with the injection pressure. As shown in Fig. 15(d), both permeability ratios decrease as the kerogen size increases. As shown in Fig. 15(e), the maximum permeability ratio remains almost constant while the equilibrium permeability ratio decreases linearly with an increase in the Biot coefficient.

4.3. Investigation of permeability evolution under conditions of constant stress

4.3.1. Evolution of permeability under conditions of constant stress

The evolution of permeability and nanotube radius for the cases of non-adsorbing (He) and adsorbing gases (CO_2) under conditions of constant stress are illustrated in Fig. 16 and Fig. 17, respectively. Three distinct stages are observed for both gases: (1) Permeability Increase. The permeability increases due to the increased gas pressure in the nanotube. This is a transient process due to the relatively high permeability of the nanotube. This stage is the same as the first stage under conditions of constant volume, and can be considered as a local behavior; (2) Permeability Decrease. In this stage, the permeability decreases because of the local swelling of kerogen as the gas molecules adsorb on the nanotube surface and diffuse into the kerogen. In this process, the nanotube shrinks. This is also a local behavior as the gas-invaded area surrounds the nanotube; and (3) Permeability Recovery. The permeability increases as the gas molecule diffuses further into the kerogen until the gas fills the entire control volume. The control volume swells, as does the nanotube, because of the constant stress boundary conditions. In this process, the external boundaries control the behavior and the process can be considered as a global behavior.

The contributions of different mechanisms under conditions of constant stress are illustrated in Fig. 18. It can be observed that: (1) Similar with conditions of constant volume, the radius increase stage is mainly caused by the local strain in the nanotube; (2) the local swelling of the kerogen matrix due to gas adsorption and diffusion is the main contributor to the decrease in permeability; and (3) the global swelling of the control volume leads to the recovery stage increasing the
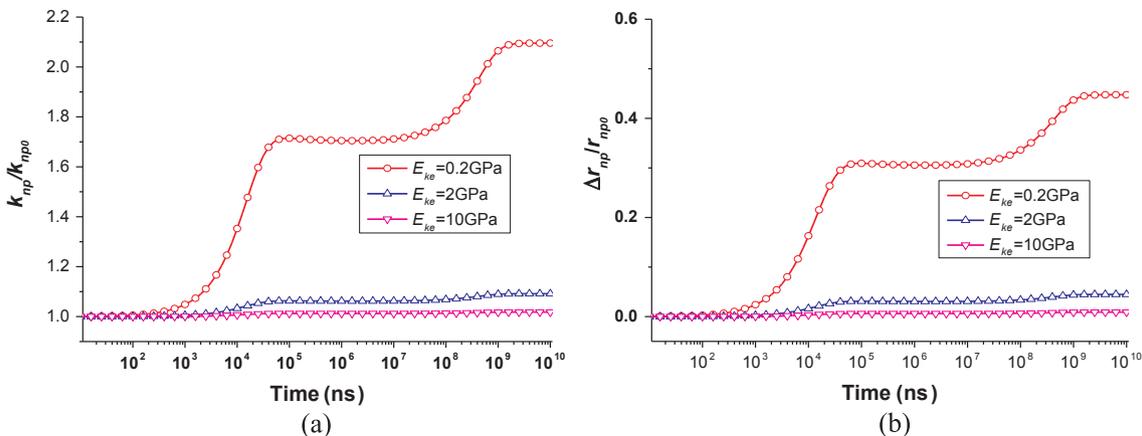
Fig. 19. Evolution of (a) permeability and (b) nanotube radius for the homogeneous distribution of Young's modulus under conditions of constant stress.
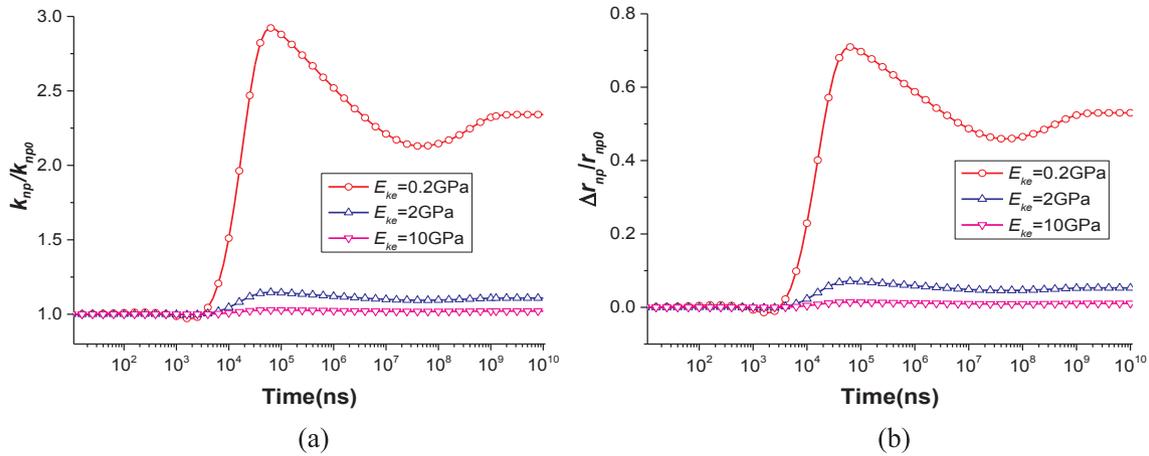
Fig. 20. Evolution of (a) permeability and (b) nanotube radius for the heterogeneous distribution of Young's modulus under conditions of constant stress.
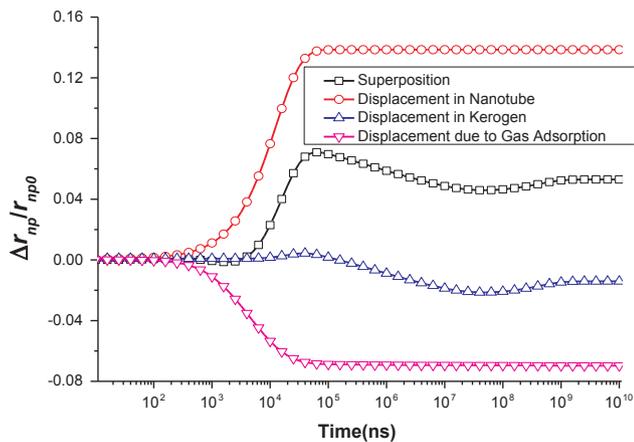
Fig. 21. Contributions of different mechanisms for a heterogeneous distribution of Young's modulus at E_{ke} = 2 GPa under conditions of constant stress.

permeability. That is because that the kerogen matrix swells outside under conditions of constant stress rather than swells inside under conditions of constant volume.

4.3.2. Investigation of Young's modulus under conditions of constant stress

The evolution of permeability and nanotube radius for the homogeneous and the heterogeneous distribution of the Young's modulus under conditions of constant stress are illustrated in Fig. 19 and Fig. 20, respectively. By comparing Fig. 19 with Fig. 20, we find that the permeability decrease stage is more apparent for the case of the heterogeneous modulus. To determine the reason, the contributions of different mechanisms to the variation of nanotube radius for the heterogeneous modulus are illustrated in Fig. 21. It can be seen that: (1) similar to the case of a homogeneous distribution, the radius increase stage is mainly caused by local strain of the nanotube, and the decrease stage is caused by the local swelling of the kerogen; (2) the change to the nanotube radius is larger for a heterogeneous modulus as the kerogen matrix is softer around the nanotube; and (3) global swelling is the main contributor to the recovery stage as the gas pressure propagates throughout the entire kerogen area.

4.3.3. Sensitivity analysis under conditions of constant stress

A sensitivity analysis is conducted to investigate the impacts of important parameters under conditions of constant stress and the kerogen matrix is considered to be homogeneous in this case. The simulation scenarios are the same as listed in Table 3 and the results are shown in Fig. 22. Notably, the inflection point permeability ratio representing the degree of nanotube local strain, the minimum

permeability ratio representing the degree of decrease stage caused by the local strain of kerogen matrix, and the equilibrium permeability ratio representing the degree of global swelling are shown.

The inflection point permeability ratio, the minimum permeability ratio and equilibrium permeability ratio all decline with increased adsorption strain as shown in Fig. 22(a). This is due to the fact that the adsorption strain results in local swelling of the kerogen matrix reducing the nanotube radius. The adsorption strain has little impact on the decreasing-permeability stage as the difference between the inflection point permeability ratio and the minimum permeability ratio is retained invariant with the increased adsorption strain. Similar to the condition of constant volume, the diffusion coefficient of the kerogen (D_{ke}) only affects the process in reaching the new equilibrium state rather than the magnitudes as shown in Fig. 22(b). The decrease stage is more apparent when the diffusion coefficient is small. That is mainly because the low diffusion coefficient slows the transition from local deformation to global deformation therefore the local strain of the kerogen matrix, inducing the decrease stage, is more apparent. The three ratios have linear relationships with the injection gas pressure as shown in Fig. 22(c). Taking the equilibrium permeability ratio as an example, the permeability ratio increases from 1 to 1.16 when the injection pressure is increased from 5 MPa to 50 MPa. While the injection pressure has little impact on the decrease stage as the difference between the inflection point permeability ratio and minimum permeability ratio has no relationship with the injection pressure. Fig. 22(d) illustrates the impact of kerogen length on the evolution of permeability. Kerogen size controls how long the decrease stage endures. This characteristic leads to the hypothesis that the decrease stage is directly related to the increased kerogen volume and that more local strain of the kerogen matrix is expected under conditions of large kerogen volume. Comparing Fig. 22(e) and Fig. 15(e), we can find that the impact of the Biot coefficient on the equilibrium permeability ratio is the reverse of that under conditions of constant volume. This demonstrates that the impact of the Biot coefficient is regulated by the external boundaries.

4.4. Why shale permeability changes under constant effective stresses

The enigmatic behavior of shale permeability as shown in Fig. 1 is consistent with these prior model results (e.g. Fig. 22(d)). During gas injection, the gas pressure in the fracture immediately reaches the injection pressure due to its high permeability. Conversely, the kerogen matrix system takes a very long time to reach the injection pressure due to its low diffusivity. Mass and stress transfers occur because of the contrast of transport capabilities between the two components (fracture and matrix). In experiments, we maintain the effective stress in the fracture system constant while the mass and effective stress transfers
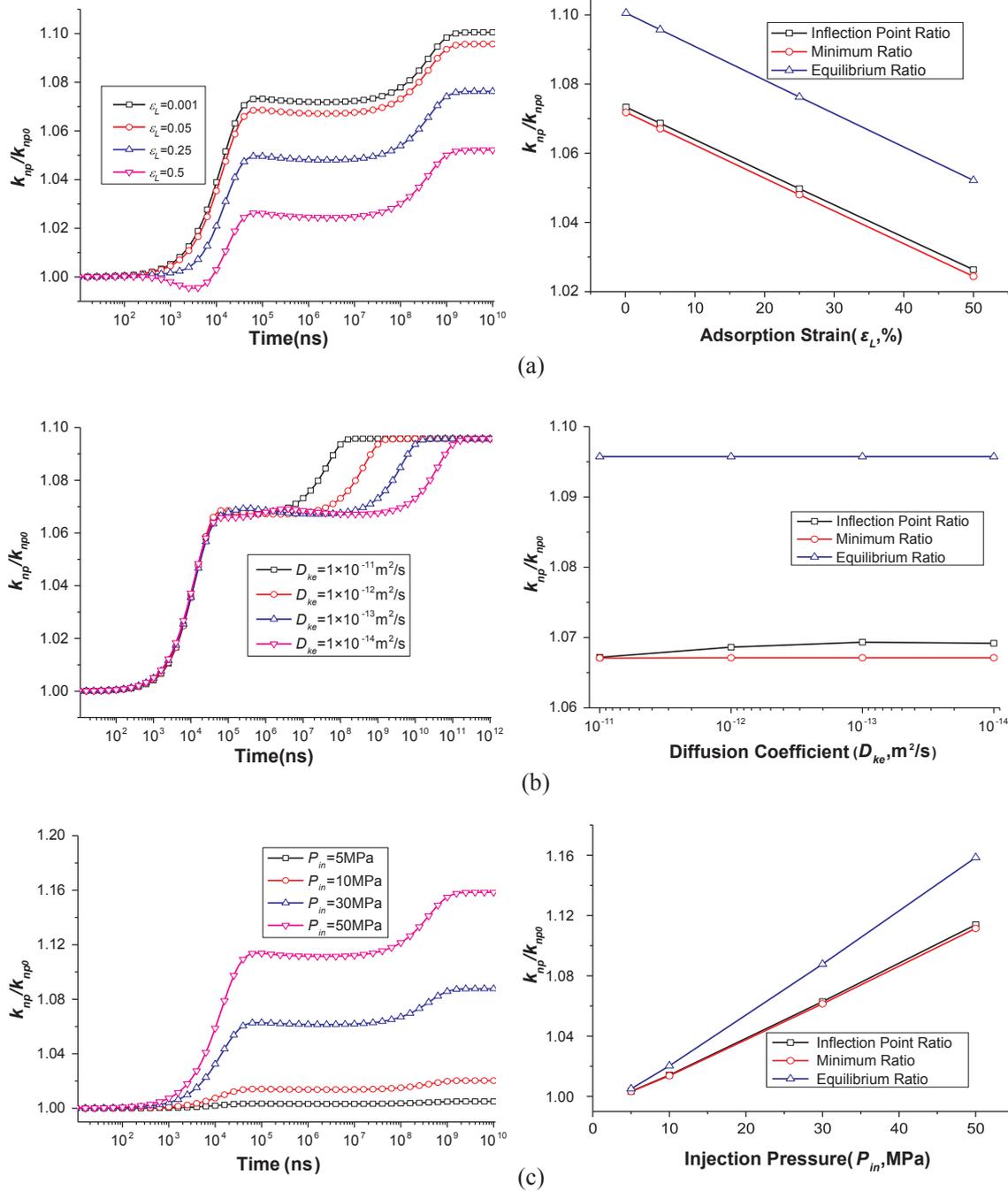
Fig. 22. Influences of (a) adsorption strain (b) kerogen diffusion coefficient (c) injection pressure (d) kerogen length and (e) kerogen Biot coefficient on permeability evolution under conditions of constant stress.

between the fracture and matrix systems may never reach a steady state. It is the effective stress in the matrix system that determines the evolution of shale permeability. This explains why shale permeability changes under constant effective stresses.

As shown in Fig. 22(d), the size of the kerogen packet controls the duration of the decrease stage of permeability. If the kerogen packet is sufficiently large, the effective stress in the matrix system may never reach a steady state. Under this condition, the shale permeability is controlled primarily by the local strain. For the case of gas injection, the local matrix swelling results in a reduction of pore volume. This reduction of pore volume decreases the shale permeability. If the matrix diffusivity is very small, similar conclusions can be drawn as shown in Fig. 22(b). Therefore, if the kerogen matrix is large or its diffusivity is low, the matrix local strain plays the most significant role and the

permeability evolution replicates experimental observations during gas injection as shown in Fig. 1. During the early period of gas injection (low gas pressure), the gas invaded-area is in the vicinity of the fracture and the permeability decreases because of the local swelling strain of the kerogen matrix. As time progresses, the gas diffuses further into the kerogen matrix and the governing mechanism of permeability evolution transforms from local deformation to global deformation.

5. Model verification against experimental observations

5.1. Experimental observations

Guo [77] reports experiments using a tri-axial apparatus capable of measuring permeability of shale samples as shown in Fig. 23. This tri-

(d)

(e)
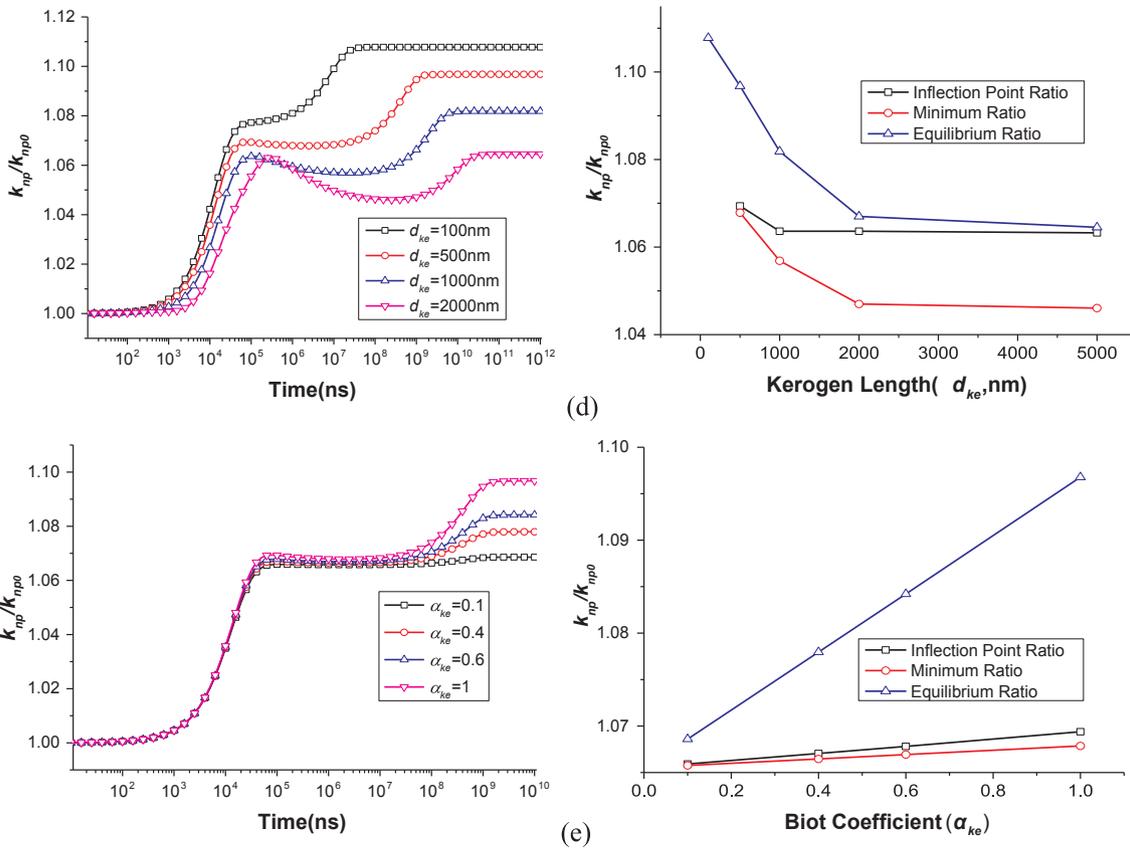
Fig. 22. (*continued*)
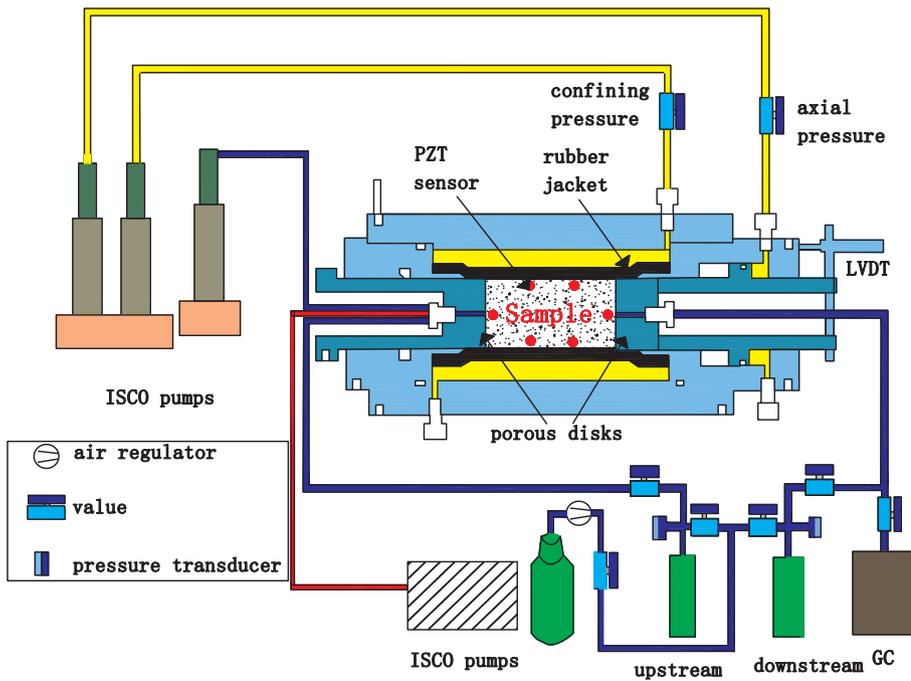
Fig. 23. Schematic of experimental set-up.

axial core holder accepts membrane-sheathed cylindrical samples and applies a prescribed path of effective stresses. The pressure transient method [78] is used to measure the low permeability. The shale sample is cylindrical of 2.5 cm in diameter and 5 cm in length and comprises Green River shale (Utah, USA).

A series of permeability measurements are reported for the sample at invariant confining pressure and incremented pore pressure.

Experimental conditions are confining with axial stresses of 7 MPa and the pore pressure increases from 1 MPa to 5 MPa step by step during the experiment. The permeants are non-adsorbing He and adsorbing CO_2 to investigate the impact of the transition from local behavior to global behavior on permeability change. The experiment results are presented in Fig. 24.

The experimental results demonstrate that the permeability
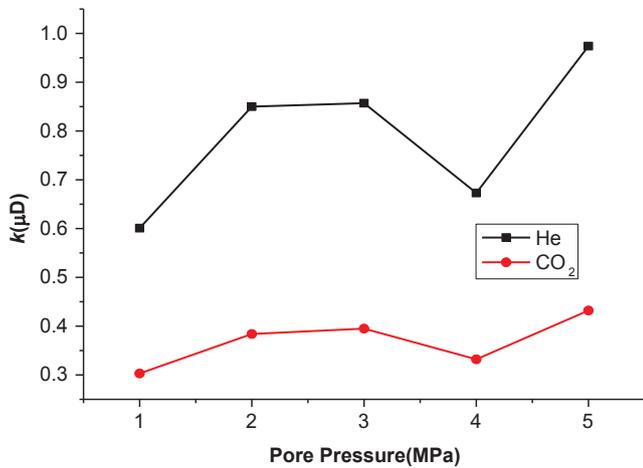
Fig. 24. Evolution of permeability for non-adsorbing (He) and adsorbing gases (CO_2).

Table 4
Parameters assumed for the verification model.

Symbol	Description	Value	Unit
r_{np}	Nanotube radius	2	nm
d_{ke}	Kerogen length	500	nm
ε_L	Langmuir strain constant	0.05 (CO_2), 0 (He)	–
V_L	Langmuir volume constant	0.03 (CO_2), 0 (He)	m³/kg
P_L	Langmuir pressure constant	5	MPa

evolution of the shale matrix is closely linked with the transition from local deformation to global deformation. As discussed in the conceptual model, the evolution of permeability is dynamic and experiences three stages under conditions of constant stress. In the permeability-increasing stage, the fracture (nanotube) voids immediately fill with gas. This inflates the fractures (nanotubes) and increases the permeability. In the permeability-decreasing stage, the gas invaded-area and local swelling strain of the kerogen are limited to the fracture surface decreasing the shale permeability. In the recovery stage, gas diffuses further into the kerogen matrix which causes the swelling of the entire ensemble sample and enhances the permeability.

5.2. Model verification

The following assumptions are made for the simulation for the model verification: (1) the shale sample is assumed to consist of nanotube-kerogen units, (2) a unit can be found representing the permeability variation of the entire sample and (3) the impact of the boundary

conditions on the sample has the same impact on the representative unit. Therefore the simulation model is the same as the model shown in Fig. 8(b). The outer boundaries are confined by the invariant confining pressure of 7 MPa and the injection pressure increases from 1 MPa to 5 MPa. In the simulation model, a piecewise function including five exponential functions is used to describe the increase of injection pressure written as:

$$
\begin{cases}
p_{in}(l,t) = p_0 \, (l = 1, 0 < t < t_1) \\
p_{in}(l,t) = p_{l-1} + \Delta p_l(1-\exp(-(t-t_{l-1})/td_l)) \, (l = 2,3,4,5, t_{l-1} < t < t_l)
\end{cases}
$$

(17)

where p_0 is the initial gas pressure, p_{in} is the injection pressure varying with time, l is the index number of exponential function, t represents time, t_{l-1} is the beginning time of the lth exponential function also the end time of the previous step, $\triangle p_l$ is the gas increment between two measured steps and td_l is the characteristic time to control pressure increment. The parameters mentioned above are determined by the experiment process and the time scale is reduced to nanosecond scale at the same proportion. Each designed exponential function include increase stage and stable stage: the increase stage is applied to describe the growing injection pressure; and the measured permeability is obtained at the end of stable stage. Other parameters are as listed in Table 4.

There are three categories of permeability models in shale reservoir as discussed above: the gas-slippage-based apparent permeability approach, the effective stress based poroelasticity approach and the hybrid approach. In this work we use the apparent permeability model from Beskok and Karniadakis [42], the poroelasticity approach of Robertson and Christiansen [51] and the combined expression for comparison. The results of the comparison are shown in Fig. 25.

As shown in Fig. 25, the apparent permeability approach defines the lower boundary of the permeability evolution and the poroelasticity theory approach defines the upper boundary during the gas injection process. The hybrid approach reasonably matches the experimental observations, although the transient value is not a perfect match. Our alternative approach achieves the best match.

6. Conclusions

This study explores an alternative mechanical approach to descriptions of conventional apparent permeability to explain enigmatic behavior of shale permeability – specifically, why permeability is observed to change under constant effective stresses. Our fundamental mechanical approach is based on the theory of poroelasticity. In this approach, the evolution of permeability is controlled by the transfers of both mass and effective stress between fracture and matrix. Based on our model results, the following conclusions are drawn:

(a)

(b)
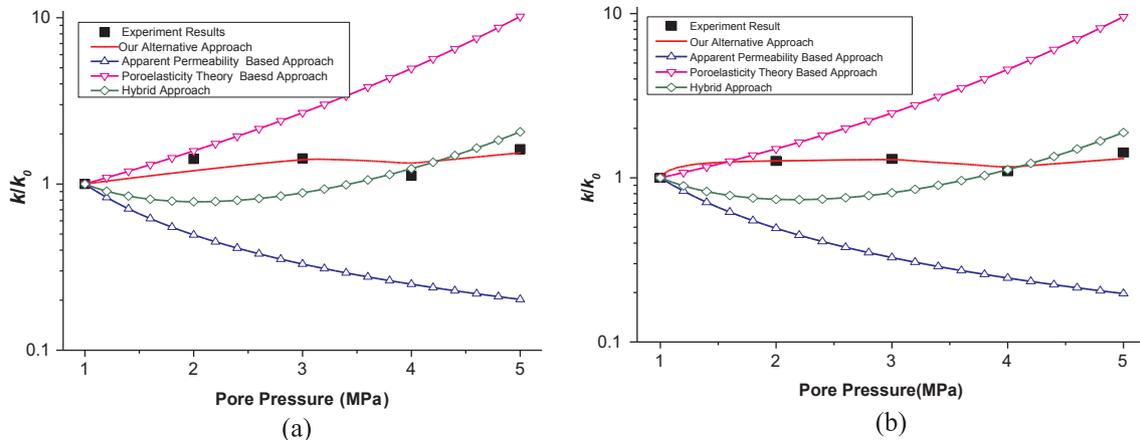
Fig. 25. Comparisons between different model results and the experimental data: (a) Helium (He) and (b) Carbon Dioxide (CO_2).

- The early stage of shale permeability is controlled primarily by the fracture system while the evolution of permeability is controlled by the interactions between fracture and matrix systems. The transfers of mass and stress between the two components (fracture and matrix) occur because of the significant contrast of transport properties. Both transfer mechanisms are important. In experiments, we maintain the effective stress in the fracture system as constant while the mass and effective stress transfers between the fracture and matrix systems may never reach a steady-state. It is the effective stress in the matrix system that determines the evolution of shale permeability. This is why shale permeability changes under constant effective stresses in the fracture system.

- The shale matrix cannot be assumed as impermeable because our model results have demonstrated its significance in the evolution of shale permeability. If the matrix is sufficiently large and its diffusivity is low, the effective stress in the matrix system may never reach a steady state. Therefore, if the kerogen matrix is large or its diffusivity is low, the matrix local strain plays a significant role and the predicted permeability evolution follows experimental observations.

Acknowledgements

References

[1] U.S. Energy Information Administration, Annual Energy Outlook 2016; 2016.
[2] Chen L, Zhang L, Kang Q, et al. Nanoscale simulation of shale transport properties using the lattice Boltzmann method: permeability and diffusivity. Sci Rep 2015;5:8089.
[3] Yang T, Li X, Zhang D. Quantitative dynamic analysis of gas desorption contribution to production in shale gas reservoirs. J Unconventional Oil Gas Resour 2015;9:8–30.
[4] Moghaddam RN, Jamiolahmady M. Fluid transport in shale gas reservoirs: Simultaneous effects of stress and slippage on matrix permeability. Int J Coal Geol 2016;163:87–99.
[5] Zhu W, Tian W, Gao Y, et al. Study on experiment conditions of marine shale gas seepage law. J Nat Gas Geosci 2016;1(2):157–63.
[6] Firouzi M, Alnoaimi K, Kovscek A, et al. Klinkenberg effect on predicting and measuring helium permeability in gas shales. Int J Coal Geol 2014;123:62–8.
[7] Cui XA, Bustin RM, Brezovski R, et al. A new method to simultaneously measure in-situ permeability and porosity under reservoir conditions: implications for characterization of unconventional gas reservoirs. In: SPE 138142 Canadian Unconventional Resources and International Petroleum Conference held in Calgary, Alberta, Canada, 19–21 October 2010.
[8] Moghadam AA, Chalaturnyk R. Analytical and experimental investigations of gas-flow regimes in shales considering the influence of mean effective stress. SPE J 2016;21(2):557–72.
[9] Pan Z, Ma Y, Danesh NN, et al. Measurement of shale anisotropic permeability and its impact on shale gas production. In: SPE 176955 SPE Asia Pacific Unconventional Resources Conference and Exhibition held in Brisbane, Australia, 9–11 November 2015.
[10] Heller R, Vermylen J, Zoback M. Experimental investigation of matrix permeability of gas shales. AAPG Bull 2014;98(5):975–95.
[11] Alnoaimi KR, Duchateau C, Kovscek AR. Characterization and measurement of multi-scale gas transport in shale core samples. In: URTEC 1920820 Unconventional Resources Technology Conference held in Denver, Colorado, USA, 25–27 August 2014.
[12] Aljamaan H, Alnoaimi K, Kovscek AR. In-depth experimental investigation of shale physical and transport properties. In: URTEC 1582140 Unconventional Resources Technology Conference held in Denver, Colorado, USA, 12–14 August 2013.
[13] Alnoaimi KR, Kovscek AR. Experimental and numerical analysis of gas transport in shale including the role of sorption. In: SPE 166375 SPE Annual Technical Conference and Exhibition held in New Orleans, Louisiana, USA, 30 September–2 October 2013.
[14] Peng S, Loucks B. Permeability measurements in mudrocks using gas-expansion methods on plug and crushed-rock samples. Mar Petrol Geol 2016;73:299–310.
[15] Ghanizadeh A, Amann-Hildenbrand A, Gasparik M, et al. Experimental study of fluid transport processes in the matrix system of the European organic-rich shales: II. Posidonia Shale (Lower Toarcian, northern Germany). Int J Coal Geol 2014;123(2):20–33.
[16] Wu W, Zoback MD, Kohli AH. The impacts of effective stress and CO2 sorption on the matrix permeability of shale reservoir rocks. Fuel 2017;203:179–86.
[17] Mehmani A, Prodanović M, Javadpour F. Multiscale, multiphysics network modeling of shale matrix gas flows. Transport Porous Med 2013;99(2):377–90.
[18] Chen C, Hu D, Westacott D, et al. Nanometer-scale characterization of microscopic pores in shale kerogen by image analysis and pore-scale modeling. Geochem Geophys Geosyst 2013;14(10):4066–75.
[19] Gad-el-Hak M. The fluid mechanics of microdevices—the freeman scholar lecture. J Fluids Eng 1999;121(1):5–33.
[20] Sherman FS. The transition from continuum to molecular flow. Annu Rev Fluid Mech 1969;1(1):317–40.
[21] Zhang X, Xiao L, Shan X, et al. Lattice Boltzmann simulation of shale gas transport in organic nano-pores. Sci Rep 2014;4:4843.
[22] Nazari Moghaddam R, Jamiolahmady M. Slip flow in porous media. Fuel 2016;173:298–310.
[23] Hadjiconstantinou N. The limits of Navier-Stokes theory and kinetic extensions for describing small-scale gaseous hydrodynamics. Phys Fluids 2006;18(11):111301–19.
[24] Shabro V, Torres-Verdín C, Javadpour F. Finite-difference approximation for fluid-flow simulation and calculation of permeability in porous media. Transport Porous Med 2012;94(3):775–93.
[25] Fathi E, Akkutlu IY. Lattice Boltzmann method for simulation of shale gas transport in kerogen. SPE J 2013;18(1):27–37.
[26] Bhattacharya DK, Lie GC. Nonequilibrium gas flow in the transition regime: a molecular-dynamics study. Phys Rev A 1991;43(2):761–7.
[27] Niu C, Hao YZ, Li D, et al. Second-order gas-permeability correlation of shale during slip flow. SPE J 2014;19(5):786–92.
[28] Tokumasu T, Matsumoto Y. Dynamic molecular collision (DMC) model for rarefied gas flow simulations by the DSMC method. Phys Fluids 1999;11(7):1907–20.
[29] Lee T, Bocquet L, Coasne B. Activated desorption at heterogeneous interfaces and long-time kinetics of hydrocarbon recovery from nanoporous media. Nat Commun 2016;7:11890.
[30] Guo C, Bai B, Wei M, et al. Study on gas flow in nano pores of shale gas reservoir. In: SPE 167179 SPE Unconventional Resources Conference Canada held in Calgary, Alberta, Canada, 5–7 November 2013.
[31] Darabi H, Ettehad A, Javadpour F, et al. Gas flow in ultra-tight shale strata. J Fluid Mech 2012;710(12):641–58.
[32] Roy S, Raju R, Chuang HF, et al. Modeling gas flow through microchannels and nanopores. J Appl Phys 2003;93(8):4870–9.
[33] Javadpour F. Nanopores and apparent permeability of gas flow in mudrocks (Shales and Siltstone). J Can Petrol Technol 2009;48(8):16–21.
[34] Civan F. Effective correlation of apparent gas permeability in tight porous media. Transport Porous Med 2009;82(2):375–84.
[35] Klinkenberg LJ. The permeability of porous media to liquids and gases, in drilling and production practice. In: API 41–200 Drilling and Production Practice held in New York, USA; 1 January 1941.
[36] Brown GP, Dinardo A, Cheng GK, et al. The flow of gases in pipes at low pressures. J Appl Phys 1946;17(10):802–13.
[37] Civan F, Rai CS, Sondergeld CH. Shale-gas permeability and diffusivity inferred by improved formulation of relevant retention and transport mechanisms. Transport Porous Med 2011;86(3):925–44.
[38] Letham EA. Matrix permeability measurements of gas shales: gas slippage and adsorption as sources of systematic error [Ph.D. dissertation]. Vancouver, Canada: University of British Columbia; 2011.
[39] Sinha S, Braun EM, Determan MD, et al. Steady-state permeability measurements on intact shale samples at reservoir conditions – effect of stress, temperature, pressure, and type of gas. In: SPE 164263 SPE Middle East Oil and Gas Show and Conference held in Manama, Bahrain, 10–13 March 2013.
[40] Naraghi ME, Javadpour F. A stochastic permeability model for the shale-gas systems. Int J Coal Geol 2015;140:111–24.
[41] Singh H, Javadpour F. Langmuir slip-Langmuir sorption permeability model of shale. Fuel 2016;164:28–37.
[42] Beskok A, Karniadakis GE. A model for flows in channels, pipes, and ducts at micro and nano Scales. Microscale Thermophys Eng 1999;3(1):43–77.
[43] Beskok A, Karniadakis G, Trimmer W. Rarefaction and compressibility effects in gas microflows. J Fluid Eng-T ASME 1996;118(3):448–56.
[44] Florence FA, Rushing J, Newsham K, et al. Improved permeability prediction relations for low permeability sands. In: SPE 107954 Rocky Mountain Oil & Gas Technology Symposium held in Denver, Colorado, USA, 16–18 April 2007.
[45] Gray I. Reservoir engineering in coal seams: part 1-The physical process of gas storage and movement in coal seams. SPE Reservoir Eng 1987;2(1):28–34.
[46] Seidle JP, Jeansonne MW, Erickson DJ. Application of matchstick geometry to stress dependent permeability in coals. In: SPE 24361 SPE Rocky Mountain Regional Meeting held in Casper, Wyoming, USA, 18–21 May 1992.
[47] Chen D, Pan ZJ, Ye ZH. Dependence of gas shale fracture permeability on effective stress and reservoir pressure: model match and insights. Fuel 2015;139:383–92.
[48] McKee CR, Bumb AC, Koenig RA. Stress-dependent permeability and porosity of coal and other geologic formations. SPE Form Eval 1988:81–91.
[49] Palmer I, Mansoori J. How permeability depends on stress and pore pressure in coalbeds: a new model. In: SPE 36737 SPE Annual Technical Conference and Exhibition held in Denver, Colorado, 6–9 October 1996.
[50] Shi JQ, Durucan S. Drawdown induced changes in permeability of coalbeds: A new interpretation of the reservoir response to primary recovery. Transport Porous Med 2004;56(1):1–16.
[51] Robertson EP, Christiansen RL. A permeability model for coal and other fractured, sorptive-elastic media. In: SPE 104380 SPE Eastern Regional Meeting held in Canton, Ohio, USA, 11–13 October 2006.

[52] Zhang HB, Liu J, Elsworth D. How sorption-induced matrix deformation affects gas flow in coal seams: a new FE model. Int J Rock Mech Min Sci 2008;45(8):1226–36.

[53] Liu J, Chen Z, Elsworth D, et al. Evaluation of stress-controlled coal swelling processes. Int J Coal Geol 2010;83(4):446–55.

[54] Peng Y, Liu J, Wei M, et al. Why coal permeability changes under free swellings: New insights. Int J Coal Geol 2014;133:35–46.

[55] Peng Y, Liu JS, Pan ZJ, et al. A sequential model of shale gas transport under the influence of fully coupled multiple processes. J Nat Gas Sci Eng 2015;27:808–21.

[56] Wang H, Marongiu-Porcu M. A unified model of matrix permeability in shale gas formations. In: SPE 173196 SPE Reservoir Simulation Symposium held in Houston, Texas, USA, 23–25 February 2015.

[57] Cao P, Liu JS, Leong YK. Combined impact of flow regimes and effective stress on the evolution of shale apparent permeability. J Unconventional Oil Gas Resour 2016;14:32–43.

[58] Wei MY, Liu JS, Feng XT, et al. Evolution of shale apparent permeability from stress-controlled to displacement-controlled conditions. J Nat Gas Sci Eng 2016;34:1453–60.

[59] Fink R, Krooss BM, Gensterblum Y, et al. Apparent permeability of gas shales – Superposition of fluid-dynamic and poro-elastic effects. Fuel 2017;199:532–50.

[60] Dong JJ, Hsu JY, Wu WJ, et al. Stress-dependence of the permeability and porosity of sandstone and shale from TCDP Hole-A. Int J Rock Mech Min Sci 2010;47(7):1141–57.

[61] Etminan SR, Javadpour F, Maini BB, et al. Measurement of gas storage processes in shale and of the molecular diffusion coefficient in kerogen. Int J Coal Geol 2014;123:10–9.

[62] Swami V, Settari A. A pore scale gas flow model for shale gas reservoir. In: SPE 155756 SPE Americas Unconventional Resources Conference held in Pittsburgh, Pennsylvania, USA, 5–7 June 2012.

[63] Detournay E, Cheng HD. Fundamentals of poroelasticity. Anal Des Methods 1993;140(1):113–71.

[64] Karacan CÖ. Heterogeneous sorption and swelling in a confined and stressed coal during CO2 injection. Energy Fuels 2003;17(6):1595–608.

[65] Karacan CÖ. Swelling-induced volumetric strains internal to a stressed coal associated with CO2 sorption. Int J Coal Geol 2007;72(3–4):209–20.

[66] Day S, Fry R, Sakurovs R. Swelling of Australian coals in supercritical CO2. Int J Coal Geol 2008;74(1):41–52.

[67] Izadi G, Wang S, Elsworth D, et al. Permeability evolution of fluid-infiltrated coal containing discrete fractures. Int J Coal Geol 2011;85(2):202–11.

[68] Chen ZW, Liu J, Elsworth D, et al. Roles of coal heterogeneity on evolution of coal permeability under unconstrained boundary conditions. J Nat Gas Sci Eng 2013;15:38–52.

[69] Sun H, Chawathe A, Hoteit H, et al. Understanding shale gas flow behavior using numerical simulation. SPE J 2015;20(1):142–54.

[70] Huang T, Guo X, Chen FF. Modeling transient flow behavior of a multiscale triple porosity model for shale gas reservoirs. J Nat Gas Sci Eng 2015;23:33–46.

[71] Ross DJK, Bustin RM. The importance of shale composition and pore structure upon gas storage potential of shale gas reservoirs. Mar Petrol Geol 2009;26(6):916–27.

[72] Wu KL, Chen Z, Li X, et al. A model for multiple transport mechanisms through nanopores of shale gas reservoirs with real gas effect-adsorption-mechanic coupling. Int J Heat Mass Trans 2016;93:408–26.

[73] Eliyahu M, Emmanuel S, Day-Stirrat RJ, et al. Mechanical properties of organic matter in shales mapped at the nanometer scale. Mar Petrol Geol 2015;59(59):294–304.

[74] Shukla P, Kumar V, Curtis M, et al. Nanoindentation studies on shales. In: ARMA 2013–578 47th U.S. Rock Mechanics/Geomechanics Symposium held in San Francisco, California, USA, 23–26 June 2013.

[75] Chen F, Duan Y, Wang K, et al. A novel pressure transient response model considering multiple migration mechanisms in shale gas reservoir. J Nat Gas Sci Eng 2015;22(22):321–34.

[76] Shabro V, Torres-Verdin C, Sepehrnoori K. Forecasting gas production in organic shale with the combined numerical simulation of gas diffusion in kerogen, Langmuir desorption from kerogen surfaces, and advection in nanopores. In: SPE 159250 SPE Annual Technical Conference and Exhibition held in San Antonio, Texas, USA, 8–10 October 2012.

[77] Guo F. Experimental investigation of shale permeability [Master thesis]. Perth, Australia: The University of Western Australia; 2014.

[78] Brace WF, Walsh JB, Frangos WT. Permeability of granite under high pressure. J Geophys Res 1968;73(6):2225–36.